ADVANCES IN NUCLEAR SCIENCE AND APPLICATIONS

Volume 2, No. 1 (2026), P. 61-78

Microstructure of dysprosium hafnate after sequential irradiation with heavy and light ions

M.S. Staltsov *,[1], D.P. Shornikov[1], A.V. Tenishev[1], I.I. Chernov[1], A.A. Urusov[2], A.A. Mokrushin[2], V.D. Risovany[2], E.A. Petrov[2], S.V. Chuvikov[2]

[1]National Research Nuclear University MEPhI, Moscow, Russia

[2] JSC Research Institute NPO Luch, Podolsk, Moscow Region, Russia

e-mail: m.staltsov@gmail.com

DOI: 10.63907/ansa.v2i1.73
Received: 08 February 2026

Abstract

The paper presents the results of a study on the microstructure of dysprosium hafnate $0.5Dy_2O_30.5HfO_2$ after irradiation with heavy and light ions. Tablet samples of the studied material were prepared using traditional powder metallurgy methods (pressing a powder mixture followed by sintering at 1800°C). Irradiation was carried out sequentially (5 cycles) with Ni^{4+} ions with an energy of 11.5 MeV and He^+ ions with energies of $0.8 - 1.4$ MeV to damaging doses of $20 - 300$ dpa and helium content of 84 appm He/dpa at 350°C and 550°C. The microstructure was studied using transmission electron microscopy. It has been revealed that radiation-induced porosity is formed in all the studied samples, with the size of pores/bubbles slightly increasing in size and density with increasing the dose and irradiation temperature. The maximum swelling was observed in the sample irradiated up to 300 dpa at 550°C. The swelling of all samples remains within 0.1%, which indicates the high radiation resistance of dysprosium hafnate.

1 Introduction

Absorbing elements used in modern nuclear reactors must meet a large number of different criteria, the most important of which is the ability to ensure effective control of nuclear reactions. In this regard, they are subject to strict requirements, the most important of which is high radiation resistance, while the stability of structure and dimensions under the influence of high-energy particles is extremely important, both at normal operating temperature and at elevated temperatures.

The classic functional material for absorbing elements of modern reactors is boron carbide [1–3]. However, boron carbide has significant drawbacks, especially in terms of radiation resistance. Therefore, recently scientists have been actively investigating other possible materials with good absorbing capability. One of them may be a ceramic material based on dysprosium hafnate. Overall, some of the most promising absorbing materials are fluorite-type solid solutions in the $Dy_2O_3 - HfO_2$ system [1]. The compounds formed in this system contain two neutron-absorbing elements: Dy and Hf, which further enhance the material's physical efficiency. Using dysprosium hafnate granules allows increasing the absorber's density to $70 - 75\,\%$ of the theoretical density. The $Dy_2O_3 - HfO_2$ compound possesses higher density, good thermophysical properties, sufficient physical efficiency, and radiation resistance. Despite the demonstrated high radiation resistance of dysprosium hafnate, the study of its irradiation-induced swelling remains important, which may, in particular, be associated with the accumulation of helium and other products resulting from nuclear-physical reactions and the formation of radiation-induced pores in the structure of absorbing materials [1].

For the rapid assessment of swelling of the materials in nuclear reactor active zones, simulation irradiation using charged particle accelerators is widely used. Structural materials [3–7], fuel [8, 9], and functional materials [10, 11] are irradiated with light and heavy ions.

Simulation irradiation with charged particle accelerators has several advantages compared to reactor irradiation: a high rate of dose accumulation and implanted atom concentration; controlled irradiation conditions; no material activation [4–12]. Simulation ion irradiation allows the rapid identification of qualitative effects of accumulated radiation damage and nuclear reaction products (helium) in the material and provides a quantitative assessment of the parameters of the resulting porosity [4, 13, 14]. The aim of this work was to study the effect of ion irradiation on changes in the microstructure of samples of prospective absorbing materials based on the $D_{y2}O_3 - HfO_2$ system, including an analysis of radiation-induced porosity.

2 Materials and Methods

2.1 Materials and Irradiation Parameters

The study investigated promising absorber materials based on the $Dy_2O_3 - HfO_2$ system, intended for use in reactor absorbing elements. The irradiation conditions of the investigated samples are presented in Table 1.

Dysprosium hafnate tablets ($0.5Dy_2O_30.5HfO_2$) were obtained using a conventional powder metallurgy method, which includes compact pressing followed by sintering at $1800°C$. The tablet preparation involved the following technological

Table 1: Conditions of sample irradiation

Sample No., Heat treatment	Temperature, °C	Dose, dpa
$0.5D_{y2}O_30.5HfO_2$		
15, HT	350	20
9	350	100
8	350	200
1, HT	350	200
13	350	300
14	550	20
6, HT	550	100
7, HT	550	200
10, HT	550	300

steps: powder preparation, plasticizer addition, compaction, plasticizer removal, sintering, and mechanical processing.

In this study, hafnium oxide powder (HfO_2) with an average particle size of 40-60 μm and dysprosium oxide powder (Dy_2O_3) with an average particle size of 5-7 μm were used. The powder particles had an angular shape. Grinding and mixing of the oxides were carried out in a ball mill; to minimize contamination, the jar and milling media were made of WC6 cemented carbide. The milling was performed at a speed not exceeding 250 rpm, with a total duration of no more than 24 hours. A co-milling of hafnium and dysprosium oxides was applied. Due to the impact and abrasive effects and local heat-ing, oxide particles are capable of limited mutual diffusion. Additionally, the co-grinding of materials in the mill leads to additional defect formation and mechanical stresses. All of this activates the solid-phase chemical reaction and contributes to a reduction in sintering temperature and time. After grinding, the average particle size of the powders was approximately 0.8 μm.

Polyvinyl alcohol was used as a plasticizer in an amount not exceeding 1.5 wt. %.

Pressing was carried out in steel dies, with a specific pressure not exceeding 75 MPa. After pressing, the compacts retain their external shape, and no delamination cracks or chips were ob-served.

Tablet sintering was carried out in a high-temperature vacuum furnace SSHVE 1.2,5/25I2 (vacuum 10^{-5} Pa) with a tungsten heater. The samples were placed in a molybdenum container to prevent recondensation of the heater material on the tablets. In the first stage, heating was carried out up to 500°C at a rate of 5°C/min , followed by holding for at least 30 minutes to remove the binder, after which the temperature was raised to 1800°C with a hold at this temperature for at least 2 hours. After solid-phase sintering, the resulting ceramic tablets of all compositions were mechanically processed on a centerless and surface grinding machine to obtain samples of the required linear dimensions.

Irradiation was carried out on the Tandem-3M accelerator, which allows irradiation with both heavy and light ions. The irradiation of the samples was conducted in a sequential cyclic mode (5 cycles) at temperatures of 350 and 550°C : first irradiation with Ni^{4+} ions at an energy of 11.5 MeV followed by irradiation with He^{+} ions

at energies of $0.8 - 1.4$ MeV. The damaging dose during heavy-ion irradiation at the peak ranged from 20 to 300 dpa at a ratio of 84 appm He/dpa. For some of the initial samples, after pressing and annealing in a vacuum furnace, an additional an-nealing in air at $1000°C$ was performed; these samples in Table 1 are marked as HT.

2.2 Calculation of the distribution of defects and ion range through the depth of the samples

Figure 1 shows the calculated (SRIM-2013) depth distribution of implanted atoms and dis-placements per atom during the irradiation of dysprosium hafnate with Ni ions at an energy of 11.5 MeV and He ions at energies of 0.8 and 1.4 MeV.

As can be seen from the figure shown, the maximum concentrations of implanted Ni ions, He (0.8 MeV), and He (1.4 MeV) are located at depths of 3.8, 1.9, and 3 μm, respectively; the highest number of displacements per atom is noted at a depth of 3.5 μm. Thus, the most probable zone for detecting radiation-induced porosity is the zone located at a depth of 1.25 - 3.25 μm from the sample surface, containing both implanted helium and a high level of radiation-induced damage. However, preliminary studies using the TEM method showed no radiation-induced porosity in all the examined samples at depths of 2.0-5 μm from the surface. Figure 2 shows a comparison of the theoretical and experimental distributions of implanted nickel ions.

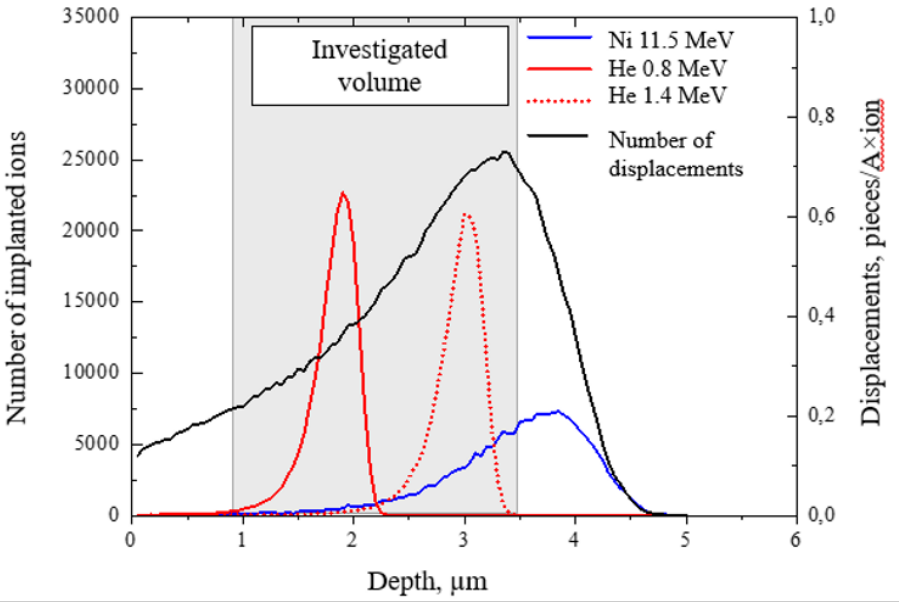

Figure 1: Calculated distribution profiles of nickel ions with an energy of 11.5 MeV, helium with ener-gies of 0.8 and 1.4 MeV, and the number of displacements per atom per incident particle (SRIM-2013) in dysprosium hafnate $0.5Dy_2O_30.5HfO_2$.

As can be seen from the figure shown, unlike the calculated value, the experimentally measured maximum nickel concentration is observed closer to the surface of the studied microsample at a depth of approximately 2.5 - 2.8 μm. This discrepancy is

not unexpected, since earlier in some studies discrepancies between the calculated data on ion penetration and experimental results had been shown [15, 16].

The studies of the microstructure and elemental composition of the cross-sections of the samples were carried out using a Tecnai G2 F20 transmission electron microscope (FEI, Netherlands) with a resolution of 0.24 nm in TEM mode (transmission electron microscopy) and 0.1 nm in STEM mode (scanning transmission electron microscopy). The images were obtained in bright-field mode (TEM mode, diffraction contrast) when capturing porosity, and in high-angle annular dark-field mode (STEM mode, Z-contrast) when constructing elemental maps and elemental distribution profiles. When studying porosity, bright-field image pairs were obtained for each investigated area in both 'defocus' and 'refocus' modes. When calculating porosity parameters from these images, the pores were considered as objects that changed their contrast when passing through focus.

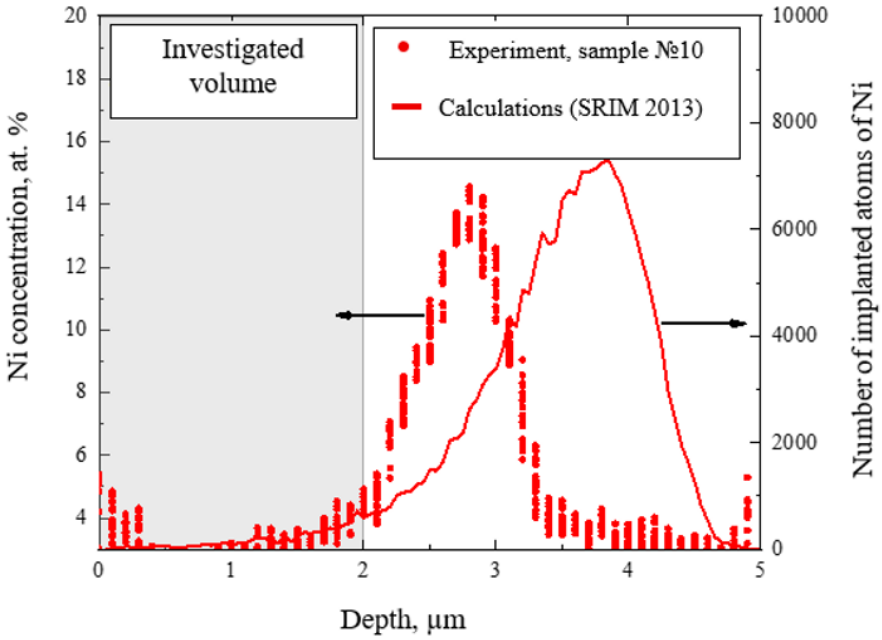

Figure 2: Calculated and experimental profiles of nickel ion distribution with an energy of 11.5 MeV in dysprosium hafnate $0.5Dy_2O_30.5HfO_2$.

The elemental composition of the samples was analyzed by the X-ray spectrometric method using an EDAX Apollo energy-dispersive spectrometer (AMETEK, USA) with a resolution of 125 eV and a sensitivity of 0.1 wt%, combined with a Tecnai G2 F20 transmission electron microscope.

3 Experimental Results

Figure 3 shows TEM images of the original $HfO_2Dy_2O_3$ sample obtained at different magnifications. As can be seen in the presented images, the microstructure of the original sample consists of a large grain with technological porosity of about ~ 2 μm. Fine porosity was not detected in the original sample, which is confirmed by the absence of objects changing their contrast when passing through the focal plane.

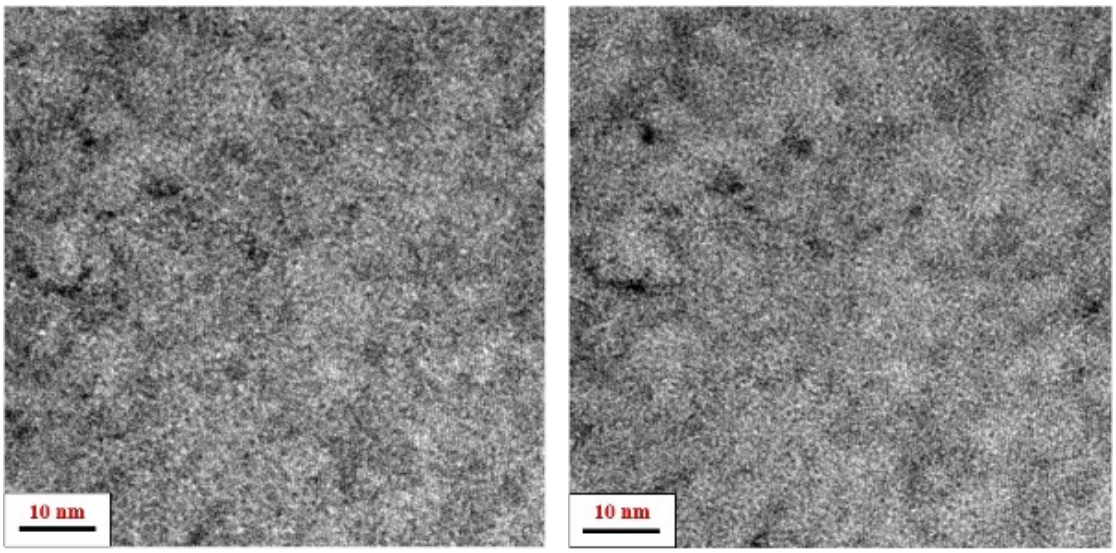

Figure 3: TEM images of the original $HfO_2Dy_2O_3$ sample (left - a) high-resolution image, underfocus mode, (right - b) is high-resolution image, overfocus mode

3.1 Microstructure of $HfO_2Dy_2O_3$ samples Irradiated at 350°C

Figure 4 shows the distribution of the main elements and the nickel implanted during irradiation along the depth of sample no.15 (20 dpa).

As can be seen in figure 4, the maximum concentration of implanted nickel is of low intensity and located at a depth of $\sim 2.6\ \mu m$, which correlates with the low irradiation dose. Due to the applied correction for the experimental nickel peak position, a detailed study of the microstructure for this sample was conducted at a distance of $\sim$ 0-2 μm from the irradiated surface of the sample.

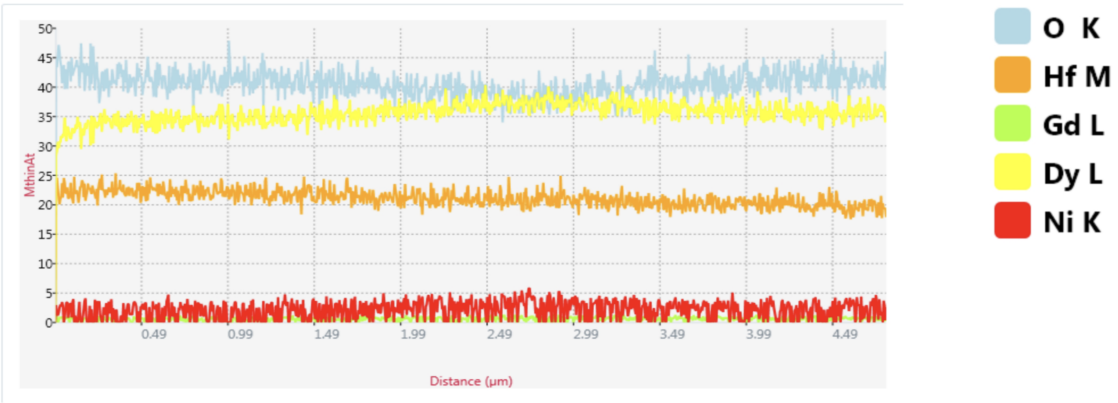

Figure 4: Distribution of the main elements and implanted nickel by depth of sample no.15 irradiated up to 20 dpa

In the near-surface layer ($\sim$ 50-100 nm) of the sample irradiated up to a dose of 20 dpa at 350°C (sample no.15 in Table 1), objects smaller than 1 nm in size were detected, distributed with high density throughout the investigated volume. However, due to their small size and the absence of contrast change when passing

through the focal plane, it is impossible to unambiguously identify these objects as radiation-induced pores/bubbles.

Figure 5 shows a pair of images ("underfocus"/"overfocus") obtained in high-resolution mode of the microstructure of areas at a depth of $\sim$775-845 nm. Individual objects have been detected, whose contrast changes when the focus is changed (highlighted with a frame in Figure 5). As a result, these objects may be pores or bubbles. The sizes of the presumed pores/bubbles are up to $\sim$1 nm; the uneven distribution of pores/bubbles throughout the area is apparently due to the small size of the objects and the relatively large thickness of the sample. The calculated swelling of this area, estimated based on the measured size and density of the pores, is $\sim$0.0025%.

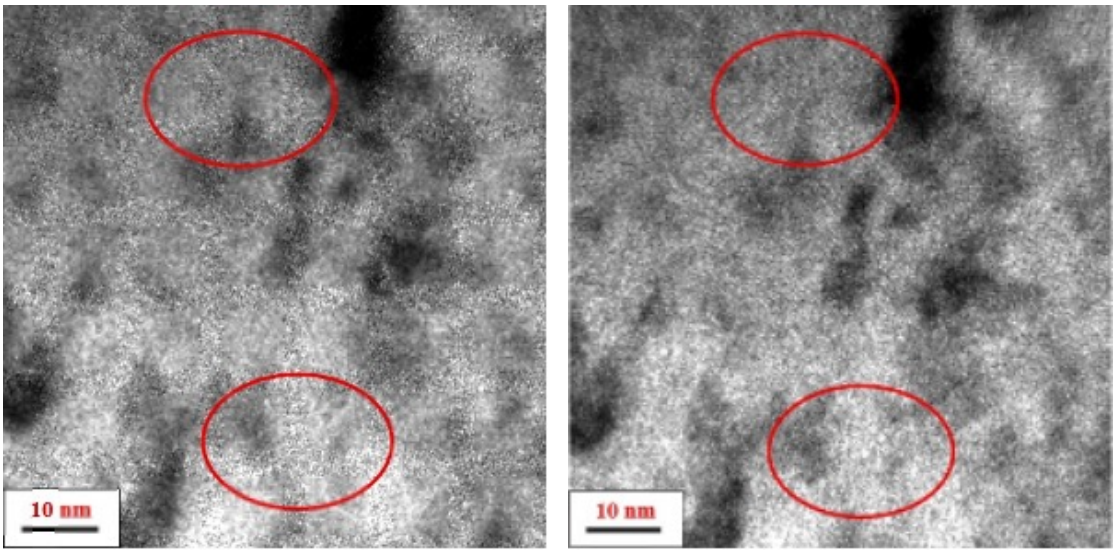

Figure 5: TEM images in high-resolution mode of the microstructure of the sample irradiated to a dose of 20 dpa, at a distance of $\sim$775-845 nm from the surface (left - a) "overfocus" mode (right - b) "underfocus" mode

At a depth of $\sim$1600 nm, isolated objects were also detected, which can be identified as pores. The size of these objects does not exceed $\sim$0.5-1 nm. Thus, in sample no. 15, irradiated to a dose of 20 dpa at 350°C, isolated objects measuring 0.5-1 nm were found in local areas, presumably being pores or bubbles. Considering their small size and low density, swelling of the irradiated layer is practically absent. The average porosity parameters for sample no.15, calculated from TEM images, are presented in Table 2. Analysis of the TEM images indicates the presence of objects that can be identified as pores/bubbles (highlighted in figure 6 a with frames). The size of these objects is $\sim$1-1.7 nm, with a higher density of these objects directly at the surface than at greater depths in this area. At greater depths from the surface of this sample, it was not possible to unambiguously identify pores/bubbles (see figure 6 b, $\sim$860-930 nm from the surface). Quite small objects with a size of up to $\sim$1-1.5 nm were detected. The same microstructure was found down to a depth of $\sim 1\ \mu m$ from the surface.

The parameters of the detected porosity, averaged over the entire depth, are presented in Table 2. The calculated swelling of the irradiated layer for sample no. 9 was approximately 0.05%. Figure 7 shows the distribution of the main elements and

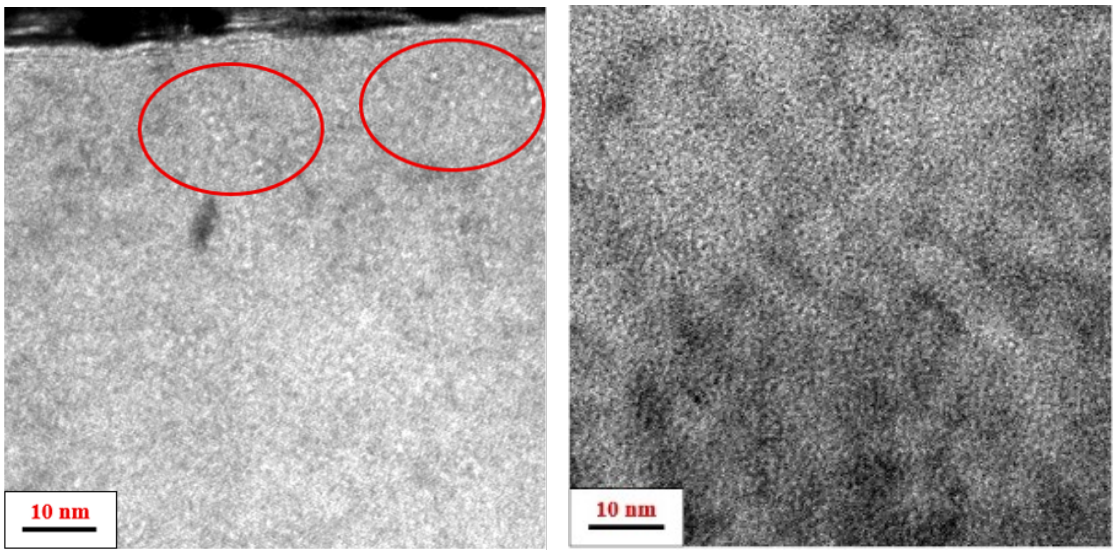

Figure 6: TEM images in high-resolution mode of the microstructure of sample no. 9, irradiated to a dose of 100 dpa, ∼0-70 nm (left - a) and (right - b) ∼860-930 nm from the surface

the nickel implanted during irradiation along the depth of sample no. 8, irradiated to a dose of 200 dpa.

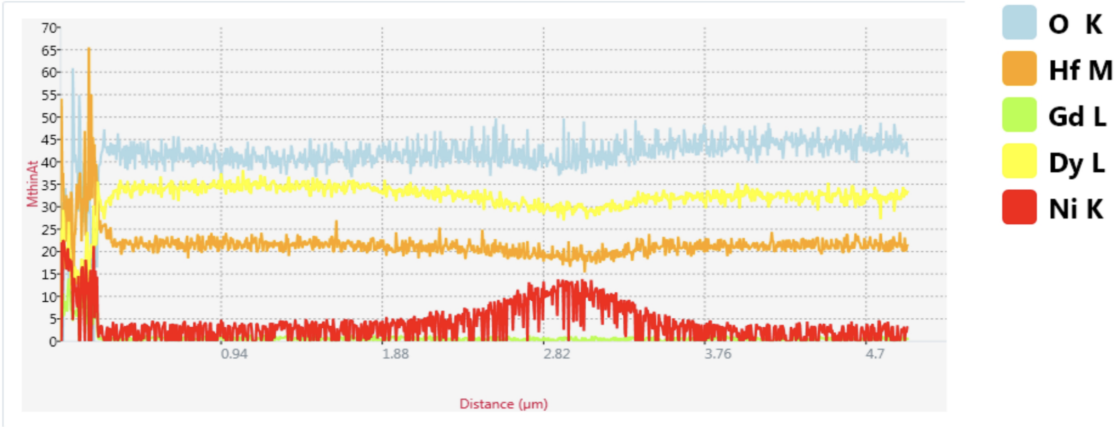

Figure 7: Distribution of major elements and nickel by depth in sample no. 8, irradiated to a dose of 200 dpa

Figure 8 shows the microstructures of the regions located in the near-surface layer of sample no. 8, irradiated up to 200 dpa at 350°C.

As can be seen in Figure 8 a, objects were detected in the near-surface layer that can be unambiguously identified as pores/bubbles with an average size of ∼1.5 nm. The density of pores/bubbles in this area is quite high (see Table 2), and there are individual regions where clusters or chains of pores/bubbles appear to have formed (highlighted by frames in Figure 8 a).

Analysis of the microstructure shown in Figure 8 b indicates that with a slight distance from the surface, the density of pores/bubbles visually increases, while the average sizes remain unchanged at approximately ∼1.5 nm. The size of individual pores/bubbles reaches ∼ nm (shown by arrows in Figure 8 b). With further removal

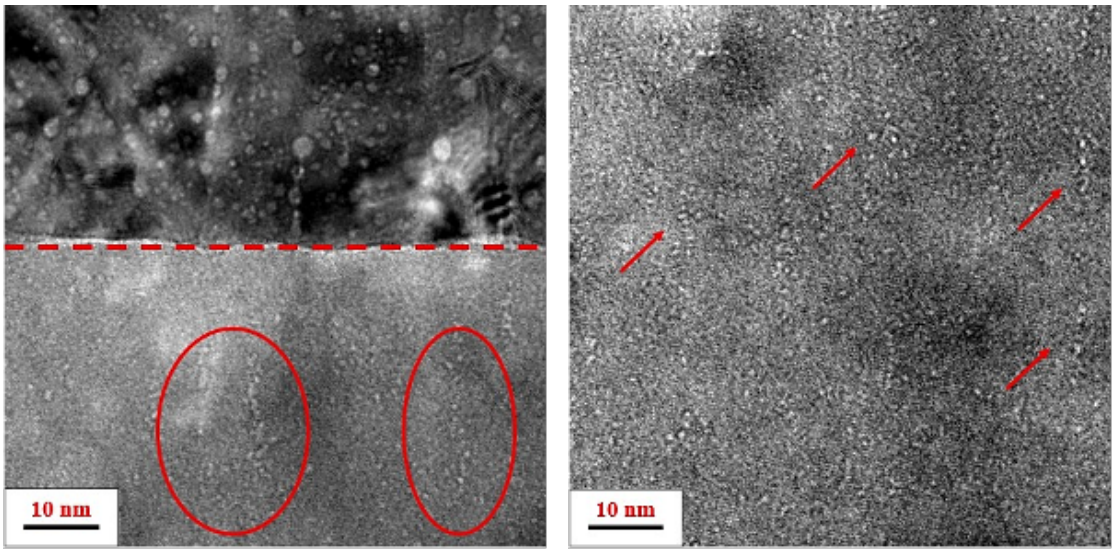

Figure 8: TEM images in high-resolution mode of the microstructure of sample no. 8, irradiated to a dose of 200 dpa, at a distance of (left - a) ∼ 0-50 nm and (right - b) ∼20-90 nm from the surface

from the surface of the sample, the overall defect pattern does not change: the density of pores/bubbles with average sizes of ∼1.5 nm remains constant.

When investigating the microstructure at depths of approximately 1450-1900 nm, it was found that as one approaches the region of the projected range of nickel, objects identified as pores/bubbles disappear, or their size becomes below the detection limit. The results of calculating the porosity parameters for sample no. 8, irradiated to a damaging dose of 200 dpa, are also presented in Table 2. The calculated swelling of the irradiated layer was approximately 0.03%. Figure 9 a shows the microstructure of the near-surface layer of sample no. 13, irradiated to a dose of 300 dpa at 350°C. Analysis of the data in figure 9 a showed the presence of pores/bubbles (highlighted with a frame) in this region with a size of approximately 1.5-2 nm and relatively low density. Figure 9 b shows the microstructure of the region at a depth of approximately 600 nm in high-resolution mode. Analysis of figure 9 shows that objects identified as pores/bubbles with sizes not exceeding ∼1-1.5 nm and relatively low density were found in the grain body at this depth. The figure shows that the studied area also contains a grain boundary (highlighted in figure 9b with a red line). In the area directly adjacent to the grain boundary, larger pores/bubbles were found, and their density is significantly higher than in the grain body. The sizes of individual, largest pores/bubbles reach ∼3-4 nm. It can be concluded that the grain boundary in dysprosium hafnate serves as an effective site for the nucleation and growth of pores/bubbles. The maximum density and size of pores/bubbles in sample no. 13 were found at a distance of ∼900-1050 nm. The microstructure is shown in Figure 10.

The size of pores/bubbles in these areas reaches ∼2-3 nm, which at high volumetric density values causes greater swelling in these areas than in other parts of sample no. 13.

At a depth of 1250-1320 nm, a fairly sparse porosity is observed with pore/bubble sizes not exceeding ∼2 nm. Thus, at depths greater than 1035 nm from the surface of the sample, the size and density of the bubbles noticeably decrease. It can be

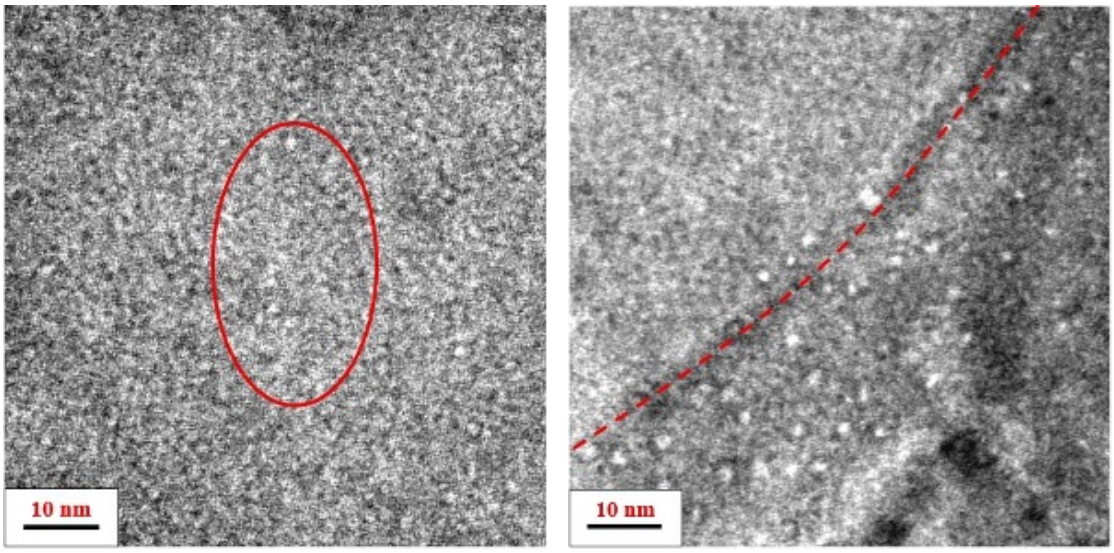

Figure 9: TEM images in high-resolution mode of the microstructure of sample no. 13, irradiated to a dose of 300 dpa, at a distance of (left - a) ∼0-70 nm and (right - b) ∼565-640 nm from the surface

concluded that in this sample, the most developed porosity corresponds to a depth of ∼900-1000 nm. Table 2 presents the results of the calculation of the porosity parameters in sample no. 13, from which it can be seen that this sample exhibits the maximum average pore/bubble size and swelling (∼0.08%) among all samples irradiated at 350°C. Figure 11 a shows a region of sample no. 14, irradiated to a dose of 20 dpa at 550°C, located directly in the near-surface layer at a depth of ∼70 nm. Data analysis indicates that objects that can be identified as pores or bubbles are detected starting from the surface of the sample and, in general, are fairly evenly distributed across the studied area. In certain regions, clusters or chains are observed. The maximum size of the detected objects is approximately 2 nm. The calculated swelling value in this area of the sample was about 0.01%. A detailed high-resolution study did not reveal significant changes in the defect microstructure of sample no. 14 with increasing depth, compared to the near-surface layer. Figure 11 b shows the microstructure of the region located at a depth of approximately 850-950 nm in sample no. 14.

As can be seen in Figure 11 b, the porosity pattern, overall, changes insignificantly with depth. Pores/bubbles with a maximum size of up to ∼2.5 nm are detected, fairly evenly and loosely distributed throughout the grain. It should be noted that visually, at a depth of ∼850-950 nm, the proportion of larger pores/bubbles is somewhat higher; the calculated swelling value for this area is 0.07%. At a distance of ∼1710-1790 nm from the surface, the maximum size of pores/bubbles in this area also reaches ∼2 nm. Compared to near-surface regions, the volumetric density of pores/bubbles has slightly decreased. Evaluating the average values of porosity and swelling parameters presented in Table 2, it can be concluded that for sample no. 14, irradiated at 550°C, the swelling value still remains quite low at ∼0.04%. Figure 12 a shows an image of the microstructure of the region at a depth of ∼150 nm of sample no. 6, irradiated up to 100 dpa at 550°C, examined in high-resolution mode. As with sample no. 14, irradiated with a significantly lower dose of helium and heavy ions, the objects identified as pores/bubbles are found directly in the near-surface

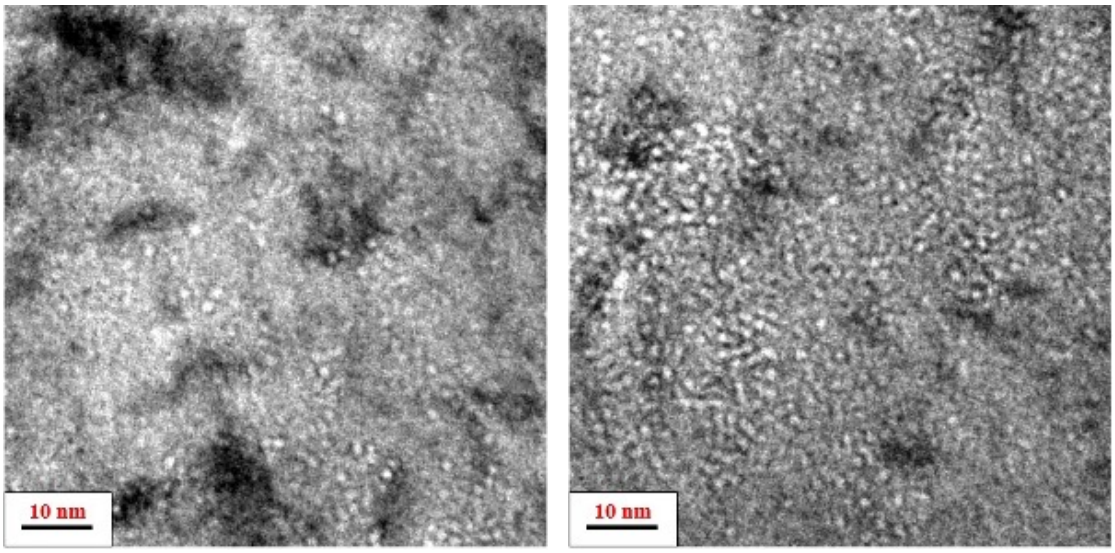

Figure 10: TEM images in high-resolution mode of the microstructure of sample no. 13, irradiated to a dose of 300 dpa, at a distance of (left - a) ∼915-985 nm and (right - b) ∼965-1035 nm from the surface

layer.

Analysis of figure 12 a allows us to assert that the pattern of defect microstructure development in the near-surface region of sample no. 6 is similar to that of sample no. 14. A relatively uniform distribution of pores/bubbles up to ∼1-1.5 nm in size was detected, with individual pores/bubbles up to 2 nm (indicated by arrows in figure 12a). Swelling in this region amounted to ∼0.05 %. A similar distribution of pores/bubbles is observed throughout the examined depth of the sample. For example, Figure 12 b shows the microstructure of sample no. 6 at a distance of ∼875-945 nm from the surface. As can be seen in figures 12 a and b, the differences in the defect structure along the projected ion path in sample no. 6 are insignificant. Only a slight decrease in the density of voids/bubbles with increasing distance from the surface can be noted. In regions where grain boundaries are present, chains of merged pores/bubbles are observed (indicated by an arrow in Figure 12 c); the size of the pores/bubbles is almost the same both at the boundary and within the grain. The length of the chain of voids/bubbles reaches several tens of nanometers. Overall, it should be noted that, as in sample no. 14, despite the increased doses during irradiation, sample no. 6 exhibits a relatively uniform distribution of pores/bubbles throughout the investigated depth. The sizes of the pores/bubbles also do not exceed the corresponding sizes for sample no. 14 and are in the range of ∼1-2 nm. Thus, at such size and density of the detected objects, no significant swelling of the irradiated layer is observed, which is reflected in Table 2; the average swelling in sample no. 6 is ∼0.04%.

In the near-surface layer, the microstructure of sample no. 10 practically does not differ from the corresponding microstructure of samples irradiated to lower doses. As can be seen from figure 13 a, the microstructure reveals objects that can be identified as pores/bubbles.

As can be seen from Figure 13 a, objects can be found in the microstructure that can be identified as pores/bubbles. The maximum size of the pores/bubbles reaches approximately 1.5 - 2 nm, and their distribution in this area of study is

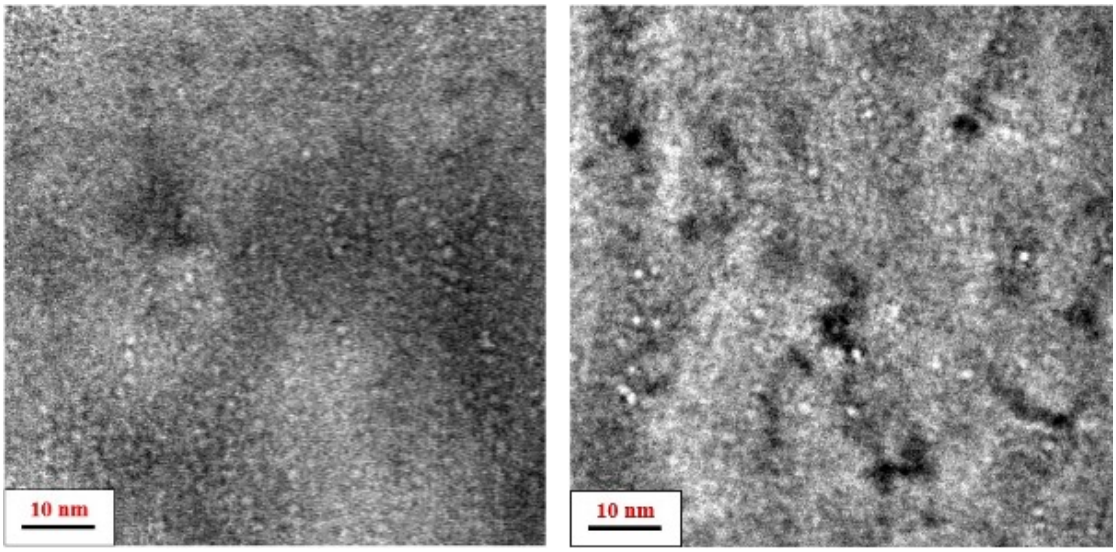

Figure 11: TEM images in high-resolution mode of the microstructure of sample no. 14, irradiated up to a dose of 20 dpa at 550°C , at a distance of (left - a) ∼20-90 nm and (right - b) ∼860-940 nm from the surface

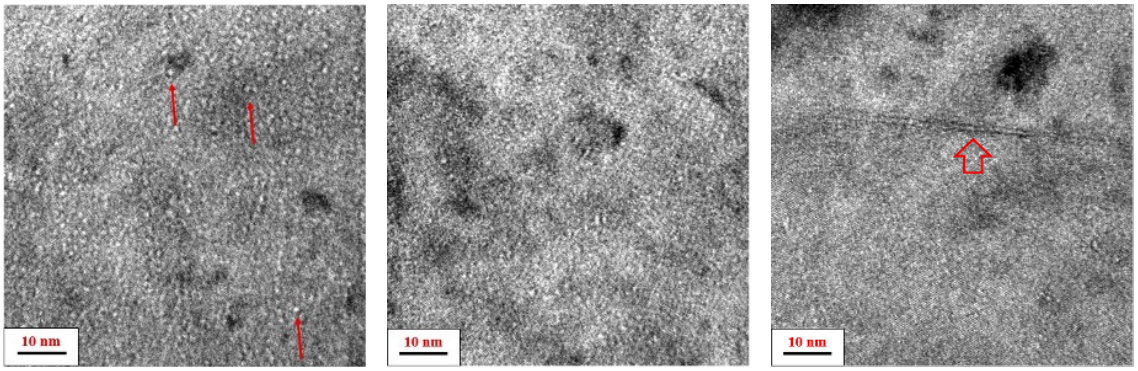

Figure 12: TEM images in high-resolution mode of the microstructure of sample no. 6, irradiated to a dose of 100 dpa, at a distance of (left - a) ∼110-175 nm, (center - b) ∼875-945 nm from the surface and near the grain boundary (right - c)

relatively uniform. However, a characteristic feature of the distribution of the detected pores/bubbles can be highlighted specifically in the near-surface layer. Chains of pores/bubbles were found in local zones of the near-surface area (highlighted by frames in Figure 13 a). Chains of pores/bubbles were not observed at greater depths from the surface. Swelling in the near-surface layer is minor, approximately 0.03 to 0.06%. In subsequent studies of the defect structure in deeper layers, a distribution of pores/bubbles similar to the previous samples was found. For example, Figure 13 b shows an image of the microstructure of an area at a depth of approximately 465 - 540 nm. It should be noted that the number of larger pores/bubbles with sizes of 1.5 - 2 nm is visually higher in the near-surface layer of sample no. 10 compared to samples irradiated at lower doses. The average density of voids/bubbles in this layer varies slightly at different irradiation doses. The swelling of this area reaches ∼0.1%. A small amount of larger pores/bubbles was also detected. Figures 13 c and 13 d show regions at depths of approximately 545 - 615 nm and 625 - 690 nm from the surface, respectively. The largest pores/bubbles in the figures are

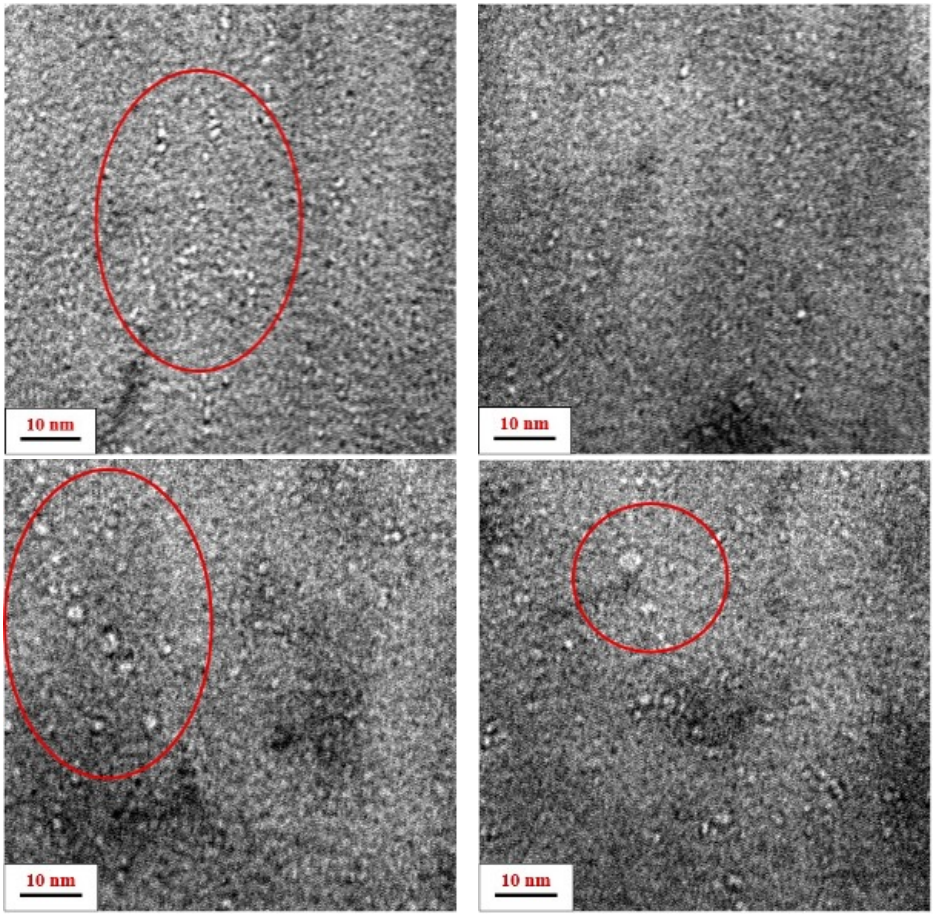

Figure 13: TEM images in high-resolution mode of the microstructure of sample no. 10, irradiated to a dose of 300 dpa, at a distance of (above left - a) ∼65-145 nm, (above right - b) ∼465-540 nm, (below left - c) ∼545-615 nm, and (below right - d) ∼625-690 nm from the surface

outlined with a red frame. Their size is 3 - 4 nm for figure 13 c and up to 5 nm for figure 13 d. Although the number of such large voids/bubbles is small, they contribute significantly to the swelling. The swelling in these areas reaches values of approximately 0.14% and 0.12%, respectively. In the deeper layers of sample no. 10, no large pores/bubbles were detected. Overall, at a distance of ∼700 -1700 nm from the surface, a microstructure similar to that of the samples irradiated at lower doses is observed. The results of the calculations of the average porosity parameters for the entire irradiated layer in sample No. 10 are presented in Table 2. It was found that swelling in sample No. 10 is the highest among all samples irradiated at 550°C and is approximately 0.11%.

4 Discussion of Results

First, it should be noted that the analysis of transmission electron microscopy data (Figures 4 and 7) shows that the amount of implanted nickel, estimated from the intensity of the experimental concentration peaks, increases with increasing irradiation dose. This confirms the consistency of the simulation experiment. At the same time, as mentioned above and shown in Figure 2, the experimental maximum

of the nickel ion distribution is no deeper than 3 μm. The vacancy maximum, according to Figure 1, should be located $\sim$0.2 - 0.5 μm closer to the surface. In this regard, the microstructure studies were concentrated in the $\sim$ 0 - 2 μm layer to avoid regions with a high concentration of implanted nickel ions. In the same layer, implanted helium atoms have the greatest effect on the structure. A comparative analysis of TEM images of the microstructures of dysprosium hafnate after irradiation at temperatures of 350 and 550°C to various doses showed (see Figures 5 - 13) that porosity formation occurred to some degree in all investigated samples. The trends in the development of porosity, however, depend on the composition of the samples, temperature, and irradiation dose. A characteristic feature of the defect microstructure development in most of the investigated samples was the formation of chains or clusters of pores/bubbles in the near-surface layer of the samples after irradiation (see Figures 6, 8, 11, and 13). This tendency is most pronounced in samples irradiated to high damaging doses. In general, the length of the chains or the volume of the clusters of pores/bubbles increases with the increasing damaging dose and the amount of implanted helium. With increasing temperature, there is a tendency for the size of the clusters of pores/bubbles to grow. The appearance of small pores/bubbles (clusters or chains) in the near-surface layer is most likely associated with surface effects as a strong sink for radiation defects and implanted helium during prolonged high-temperature irradiation. Helium and radiation vacancies diffuse to sinks at elevated temperature, one of which is the surface. Although the irradiation temperature used in this experiment is not very high for ceramics and the mobility is not that great, rather slow diffusion processes still occur. Since irradiation in this case is a prolonged process, a sufficient amount of radiation vacancies and helium accumulate in the near-surface layer. Other possible sinks for helium may be dislocations, and chain formation can occur at them. This effect has been repeatedly noted in metallic materials [17, 18]; for ceramic materials, it should be less pronounced, however, it cannot be completely excluded. This can also explain the formation of chains of pores/bubbles along grain boundaries (see Figures 9 and 12), since grain boundaries are also strong sinks for radiation defects and helium. The formation of chains of gas bubbles has been repeatedly noted, for example, in metallic alloys under helium irradiation [2, 17, 18]. Overall, it should be noted that the features of porosity formation in hafnate of dysprosium do not fundamentally differ from similar processes in metals. However, it should be understood that there are also differences, which mainly consist in the difference in the intensity of diffusion processes at the same value of homologous temperature, and, accordingly, in the sizes of the resulting objects. Table 2 presents data from the statistical analysis of porosity and swelling parameters of $HfO_2Dy_2O_3$ samples irradiated with nickel and helium ions to various doses at temperatures of 350 and 550°C.

When analyzing the data in Table 2, it should be noted that, in general, an increase in the radiation dose leads to an increase in the size of the pores/bubbles, their volumetric density, and, as a consequence, swelling. These trends are valid for both irradiation temperatures used - 350 and 550°C. The only deviation from this pattern was observed for samples 9 and 8/1, in which, with an increase in dose, the volumetric density of the pores/bubbles and their size slightly decreases, respectively. However, even in this case, the swelling of these samples coincides within the margin of error and, overall, increases with an increasing damaging dose. The decrease in

Table 2: Porosity parameters and calculated swelling values of $0.5Dy_2O_30.5HfO_2$ tablets irradiated to different doses at temperatures of 350°C and 550°C. HT is annealing in the air at 1000°C, * are samples 8 and 1 were irradiated under the same conditions

No. sample	Dose, dpa	Temperature, °C	Average diameter (d, nm.)	Average density, (m^{-3})	Swelling, %
15, HT	20	350	1.5 ± 0.3	$(1.5 \pm 0.3) \times 10^{22}$	0.003 ± 0.001
9	100	350	1.8 ± 0.5	$(1.3 \pm 0.4) \times 10^{22}$	0.05 ± 0.01
8/1*, HT	200	350	1.3 ± 0.3/ 1.3 ± 0.4	$(2.6 \pm 0.5) \times 10^{23}$/ $(2.7 \pm 0.6) \times 10^{23}$	0.03 ± 0.01 0.04 ± 0.01
13	300	350	2.1 ± 0.8	$(1.8 \pm 0.4) \times 10^{23}$	0.08 ± 0.02
14, HT	20	550	1.8 ± 0.5	$(10.0 \pm 2.0) \times 10^{22}$	0.04 ± 0.01
6, HT	100	550	1.9 ± 0.5	$(1.5 \pm 0.3) \times 10^{23}$	0.04 ± 0.01
7, HT	200	550	2.0 ± 0.4	$(1.5 \pm 0.3) \times 10^{23}$	0.07 ± 0.02
10, HT	300	550	2.1 ± 0.4	$(2.0 \pm 0.4) \times 10^{23}$	0.11 ± 0.03

the calculated values of the average size and density is apparently associated with the small size of the pores/bubbles and, consequently, statistical errors in calculating their parameters.

It was also established that an increase in irradiation temperature leads to an increase in swelling; the maximum swelling of the irradiated layer was noted for sample No. 10, irradiated at the maximum temperature (550°C) and a damaging dose of 300 dpa. The size of the detected pores/bubbles is also on average higher at a higher irradiation temperature. It was also noted that in samples irradiated at 550°C, developed porosity is observed at greater depths. In general, neither the size nor the density of pores/bubbles decreases with increasing distance from the sample surface. In samples irradiated at 350°C, the porosity developing at depth is less developed; a decrease in the size of pores/bubbles is observed with increasing depth from the surface investigated.

When considering the swelling of the investigated samples after irradiation with nickel and helium ions to various doses at temperatures of 350 and 550°C, the most important observation is that, even at extremely high damaging doses and helium concentrations, the swelling associated with porosity formation remains extremely small and does not exceed $\sim 0.10 \pm 0.02$ %.

From a general physical point of view, this result is easy to understand, considering that the irradiation temperatures of 350 and 550°C are quite low for dysprosium hafnate (< 0.4 TM, where TM is the melting temperature). At such homologous temperatures, the greatest danger in terms of structural transformation of ceramics is the possible amorphization in the case of an unfavorable ratio of damage creation rate to irradiation temperature (too high flux density or insufficient temperature) [3, 10, 19–22]. In such cases, amorphization may lead to an increase in volume and, consequently, to swelling. However, such swelling is not associated with the formation of pores or bubbles, but with the fact that the volume of the amorphous phase is larger than the crystalline phase. Nevertheless, under the experimental conditions, the amorphization of the samples was not observed, as evidenced by the results of

X-ray studies (see figure 14).

Figure 14 a shows the positions of X-ray reflections of the main components of the $Dy_2O_3HfO_2$ system and the tabular values (DB) of the lattice parameters of possible phases. In the X-ray diffraction pattern of the initial sample $0.5Dy_2O_30.5HfO_2$ (Figure 14b, black line), the main phase is dysprosium hafnate with a fluorite lattice, while traces of $\alpha - Dy_2O_3$ (cubic modification) are also detected. It should be noted that the lines of dysprosium hafnate are shifted to the left, toward smaller Bragg angles, i.e., the lattice parameter is higher compared to the tabular value. Examples of spectra from the irradiated and non-irradiated zones of sample No. 7 (550°C , 200 dpa) are also shown in the figure; for ease of perception, the spectra here and below are shifted along the ordinate axis relative to each other. It can be seen that irradiation leads to a shift of X-ray reflections (lines) and their broadening (Figure 14 b, gray line), i.e., to the refinement of the structure (BCR) and an increase in microdeformations due to an increase in defect density, as well as a change in the lattice parameter. At the same time, traces of $\alpha - Dy_2O_3$ remain, whereas in the non-irradiated zone of the same sample (Figure 14 b, blue line), the dysprosium oxide dissolves. It is worth noting that at the edge of the tablet in the initial state (Figure 14 b, purple line), dysprosium oxide was also detected, indicating a possible temperature increase over the entire surface of the tablet as a result of irradiation.

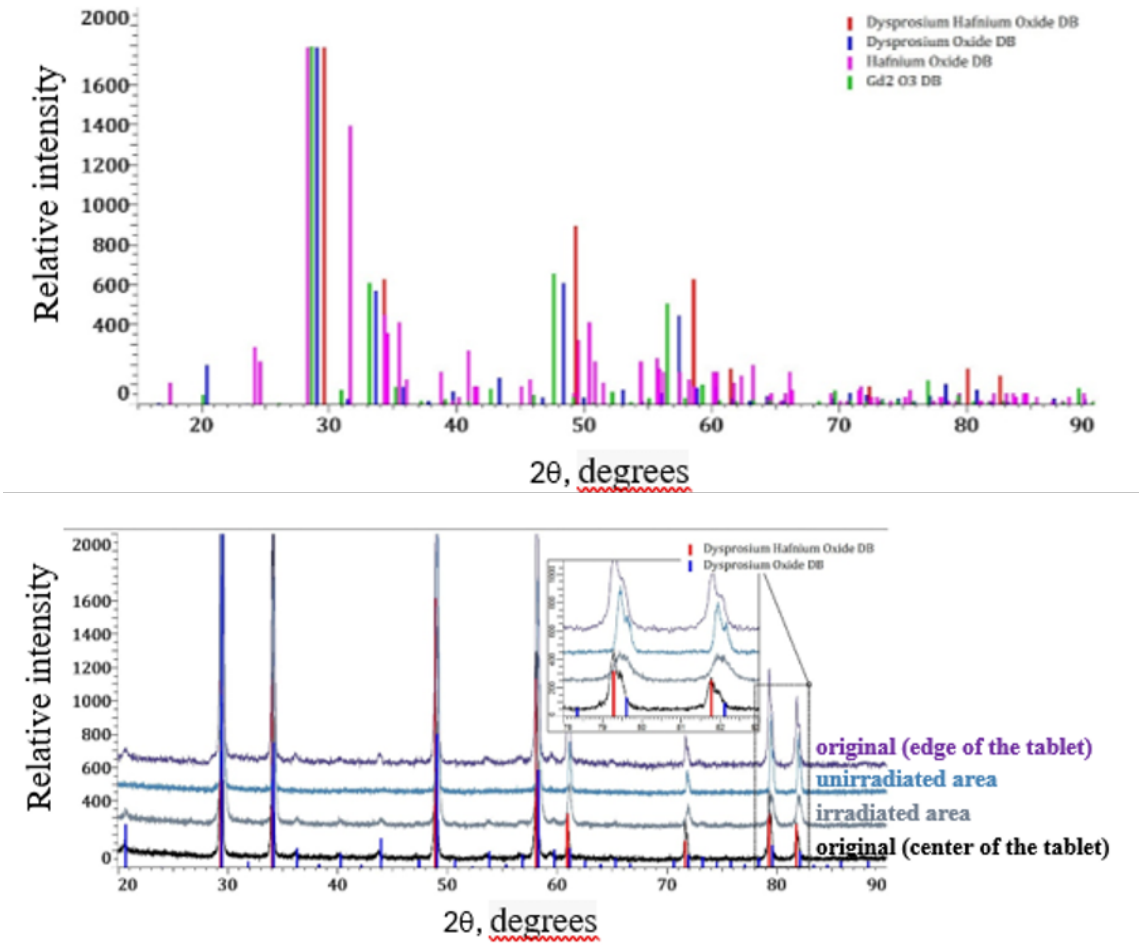

Figure 14: Tabular positions of X-ray reflections of possible phases (a) and diffraction spectra of the original sample and after irradiation (b).

Probably, the temperatures used in the experiment are still quite high, since in ceramic materials the highest degree of amorphization was observed at irradiation temperatures up to 200 - 300 °C. At higher temperatures, the amorphous state crystallizes [3]. Similar results regarding the absence of amorphization have been repeatedly observed in ceramic materials [10,19]. It is also known that the formation of vacancy porosity in ceramics is generally observed only at temperatures exceeding $\sim 0.5\ T_M$. [3, 19–22]. In general, the mechanisms of vacancy pore formation are not much different from the vacancy swelling of metallic alloys, where, as is known, swelling is associated with supersaturation by radiation-induced vacancies [2,3]. The key difference, as already mentioned above, is the higher required irradiation temperature. The observation of pore/bubble formation under experimental conditions should apparently be attributed to the capture of some vacancies by helium atoms that are insoluble in the lattice and the formation on this basis of helium-vacancy clusters. At a sufficiently high damaging dose and helium concentration, the cluster size becomes such that they turn into gas-filled voids [2,4,6,13,14,17], which can be distinguished using transmission electron microscopy. At the same time, helium does not increase the size of the detectable objects but stabilizes them.

5 Conclusions

In the study, after investigating the microstructure of $0.5Dy_2O_30.5HfO_2$ samples after irradiation with helium and nickel ions at doses of 20 - 300 dpa at temperatures of 350 and 550°C, it was found that:

1. At both temperatures used in the experiment and at any damaging doses, no amorphous structure is formed.

2. Under all experimental conditions, porosity is formed to varying degrees, with the intensity of development depending on the temperature and dose. The sizes of pores/bubbles on average increase with dose and temperature, but do not exceed 2 nm.

3. In the microstructure of many samples, chains of pores/bubbles are detected, primarily in the near-surface layer. Their size is insignificant, which may indicate insufficient development of diffusion processes at the irradiation temperature used.

4. The maximum swelling was observed for the sample irradiated to the maximum dose at the highest temperature (300 dpa at 550 °C), which is consistent with the well-known patterns of defect structure development under irradiation.

5. In general, despite the high calculated damaging dose in the experiment, all samples exhibit insignificant swelling, not exceeding $\sim 0.1\%$.

6. As a result of the conducted experiments, a preliminary conclusion can be made about the very good radiation resistance of the studied material $0.5Dy_2O_30.5HfO_2$ - there is no evidence of undesirable amorphization or significant swelling under irradiation, even at very high damaging doses.

References

[1] V. Risovany *et al.*, J. Nucl. Mater. **365**, 163 (2006).

[2] R. J. M. Konings, *Comprehensive Nuclear Materials* (Elsevier, 2012).

[3] P. Ivon, *Structural Materials for Generation IV Nuclear Reactors* (Woodhead Publishing, London, 2017), 664 p.

[4] M. Staltsov *et al.*, J. Mater. Sci. **61**, 1261 (2026).

[5] M. Ayanoglu *et al.*, J. Nucl. Mater. **570**, 153944 (2022).

[6] M. Staltsov *et al.*, J. Nucl. Mater. **461**, 54 (2015).

[7] J. H. Shin *et al.*, Nucl. Eng. Technol. **55**, 555 (2023).

[8] S. Sakib *et al.*, J. Nucl. Mater. **621**, 156394 (2026).

[9] Z. Hang *et al.*, J. Nucl. Mater. **494**, 165 (2017).

[10] S. Ghyngazov *et al.*, Ceram. Int. **49**, 37061 (2023).

[11] J. Wu *et al.*, J. Mater. Sci. Technol. **155**, 1 (2023).

[12] G. S. Was *et al.*, J. Nucl. Mater. **616**, 156065 (2025).

[13] I. Chernov *et al.*, J. Nucl. Mater. **459**, 259 (2015).

[14] M. Staltsov *et al.*, At. Energy **116**, 65 (2014).

[15] Q. Feng *et al.*, Appl. Surf. Sci. **703**, 163437 (2025).

[16] F. A. Garner, J. Nucl. Mater. **117**, 177 (1983).

[17] M. Staltsov *et al.*, Russ. Metall. **2019**, 1161 (2019).

[18] I. Chernov *et al.*, Nucl. Mater. Energy **16**, 249 (2018).

[19] P. Seo *et al.*, J. Appl. Phys. **132**, 235902 (2022).

[20] J.-M. Constantini *et al.*, J. Nucl. Mater. **564**, 153667 (2022).

[21] Y. Katoh *et al.*, J. Nucl. Mater. **448**, 448 (2014).

[22] X. Su *et al.*, J. Eur. Ceram. Soc. **46**, 118167 (2026).